


## RESEARCH ARTICLE

# Micro-electrodes for in situ temperature and bio-impedance measurement

Timothy Ka Wai Leung<sup>1</sup> | Xudong Ji<sup>1</sup> | Boyu Peng<sup>1</sup> | Gary Kwok Ki Chik<sup>1,2</sup> |  
Derek Shui Hong Siddhartha Dai<sup>1,2</sup> | Ge Fang<sup>1</sup> | Tengfei Zhang<sup>4</sup> | Xing Cheng<sup>4</sup> |  
Ka Wai Kwok<sup>1</sup> | Anderson Chun On Tsang<sup>3</sup> | Gilberto Ka Kit Leung<sup>3</sup> |  
Paddy Kwok Leung Chan<sup>1,2</sup> 

<sup>1</sup> Department of Mechanical Engineering, The University of Hong Kong, Pokfulam, Hong Kong

<sup>2</sup> Advanced Biomedical Instrumentation Centre, Hong Kong

<sup>3</sup> Department of Surgery, The University of Hong Kong, Pokfulam, Hong Kong

<sup>4</sup> Department of Materials Science and Engineering, Southern University of Science and Technology, Shenzhen, China

## Correspondence

Paddy Kwok Leung Chan, Department of Mechanical Engineering, The University of Hong Kong, Pokfulam, Hong Kong.  
Email: [pklc@hku.hk](mailto:pklc@hku.hk)

## Funding information

Hong Kong Research Grant Council, Grant/Award Number: HKU17204517

## Abstract

With fast recovery time and effective in situ tumor tissue killing ability, thermal ablation has become a popular treatment for tumors compared with chemotherapy and radiation. The thermal dose measurement of current technology is usually accompanied by monitoring a large area impedance across two ablation catheters and the localized impedance measurement is difficult to achieve. In this work, thermal-resistive sensor and impedance sensor are fabricated on the curved surface of a capillary tube with 1 mm outer diameter. The device is applied for real-time in situ tissue impedance monitoring during thermal ablation. The calibrated thermal-resistive sensors have an average temperature coefficient of resistance (TCR) of  $0.00161 \pm 5.9\% \text{ } ^\circ\text{C}^{-1}$  with an accuracy of  $\pm 0.7 \text{ } ^\circ\text{C}$ . By adding electro-polymerized PEDOT:PSS (poly(3,4-ethylenedioxythiophene)-poly(styrenesulfonate)) on the 300  $\mu\text{m}$  diameter gold electrodes, the interface impedance reduces two orders from 408 to 3.7 k $\Omega$  at 100 Hz. The Randles equivalent circuit model fittings show a two-order improvement in the electrode capacitance from 7.29 to 753 nF. In the ex vivo porcine liver laser ablation test, the temperature of the porcine liver tissue can reach 70 $^\circ\text{C}$  and the impedance would drop by 50% in less than 5 minutes. The integration of laser ablation fiber with the impedance and temperature sensors can further expand the laser ablation technique to smaller scale and for precise therapeutics.

## KEYWORDS

impedance, in situ, probes, thermal ablations

## 1 | INTRODUCTION

Thermal ablation is one of the most popular minimal invasive treatment options for cancers. By focusing on the

temperature change in a specific zone around the tumor tissue, thermal ablation can damage tissues by extreme hyperthermia or hypothermia. The destructions of the cells are due to the denaturing of proteins, the lysis of

This is an open access article under the terms of the [Creative Commons Attribution](https://creativecommons.org/licenses/by/4.0/) License, which permits use, distribution and reproduction in any medium, provided the original work is properly cited.

© 2021 The Authors. *Nano Select* published by Wiley-VCH GmbH

the cell membrane; hence the nutrient supplies of the cells would be cut off.<sup>[1-2]</sup> For patients with small lesions or fibroadenoma (2-3 cm), less risky thermal ablation is preferred instead of traumatic open surgery.<sup>[3-4]</sup> Patients will recover faster from minimal invasive surgery, and the cost of post-surgical care will be lowered. The process of thermal ablation is usually guided by computed tomography or ultrasound to locate the lesions while the ablation temperature is closely monitored by a separate thermocouple.<sup>[5]</sup> Although body tissues have different thermal tolerance,<sup>[6]</sup> at temperature below  $-40^{\circ}\text{C}$  or in excess of  $60^{\circ}\text{C}$ , most cell types will have complete necrosis.<sup>[7]</sup> In clinical surgery practice, the thermal ablation performance of the target zone will be, however, hindered by the presence of vessels nearby where the blood flow would induce a significant heat sinking effect. Vessels larger than 3 mm can potentially lead to incomplete tumor destruction by RF ablation.<sup>[8]</sup> As a result, precise temperature control and monitor in a small specific local area will be a merit for thermal ablation surgery.

Besides the increases of temperature, the electrical conductivity of the ablation site, due to cell lysis and enhancement of ion mobility, would also increase and should be monitored in real-time. To date, biopsy is the commonly used method for identifying tissue morphology and cell characteristics and it involves several preparation procedures. However, it still has a certain chance of getting false-negative results.<sup>[9-10]</sup> It would be a significant advantage if the electrical conductance of the tissues under ablation can be measured continuously in real time so that the clinicians would know when to stop the ablation for biopsy tests. It provides an immediate evaluation of the tissue condition and can provide information for the follow-up analysis. One way to evaluate the conductance of these tissues is to measure the bioimpedance of the samples under a range of a.c. frequency, and it is known as the bioimpedance spectroscopy (BIS). There are extensive studies in the dielectric properties of biological tissues,<sup>[11-17]</sup> which shows the variation of impedance response from different tissue structure. BIS technique is widely used for the advantage of fast response, label-free, low-cost, real-time measurement capabilities, etc.<sup>[18]</sup> This technique had been applied in multiple fields such as differentiating cancerous and normal tissues or cells,<sup>[14,16,19-23]</sup> tissue healing monitoring,<sup>[24-25]</sup> bone osteoporosis monitoring,<sup>[26]</sup> agricultural quality,<sup>[27]</sup> electrical impedance tomography,<sup>[15,28]</sup> cardiography.<sup>[29-31]</sup> A lot of recent works integrate bioimpedance measurement with biopsy needle to acquire electrical information at the tip of the needle.<sup>[21,32-36]</sup>

In the current work, we demonstrate a new probe with a capability of both real-time thermal monitoring and real-time impedance monitoring during thermal ablation.

Instead of using a metal needle, we used a capillary glass tube with 1 mm outer diameter. Capillary glass tube has advantages over the metal needle for its transmittance of light. Unique ablation technique such as laser ablation involves transmitting high energy laser to the target site via a glass fiber. The laser light is distributed isotopically around the applicator tip to generate rapid heating. The laser integrated capillary device can heat up the tissue to  $70^{\circ}\text{C}$  within 5 minutes and, at the same time, measure the temperature and impedance change during the heating process. Through direct photolithography patterning on capillary glass tube, we have achieved an Au temperature sensor with a width of  $10\ \mu\text{m}$  on the tissue impedance sensors, and 300 nm of PEDOT:PSS layer is electropolymerized onto the Au microelectrode surface to further reduce the interface impedance. The whole device is connected to a micro-USB port on a printed circuit board (PCB), and all signals are collected via the micro-USB. This easy-to-use, low-cost, plug-and-play ablation sensor probe can potentially broaden the applications of thermal ablation on precision therapeutics.

## 2 | RESULTS AND DISCUSSION

Figure 1 shows the detailed structural schematic of the Bio-impedance and temperature sensing probe. The PCB was designed to channel the electrical signal between the sensors and the electrochemical workstation via the micro-USB jack and the electrical signals were collected via the four independent channels. The total length of the capillary tube is 40 mm, and the maximum insertion depth of this probe is 22.5 mm. Two circular electrodes, with  $300\ \mu\text{m}$  diameter each, were patterned 3 mm apart for the impedance measurement while the Au thermal-resistive coil (thermistor) is sandwiched between the bio-impedance electrodes. The thermistor has a line width of  $10\ \mu\text{m}$ , and the total length of the coil is about 27 mm long. Longer coil length increases the total resistance and provide a larger resistance change as temperature varies. This can improve the signal to noise ratio.<sup>[37]</sup> The total length of the temperature sensor is 2.5 mm, and the temperature measured would be an averaged temperature across the length of the sensor. Compared with the works using a co-axial design of the biopsy needle, our work provides more flexible customization of electrode patterns because the whole probe surface can be used for accommodation of multiple electrode patterns. The diameter of the probe in this work is 1 mm, and it is around 20% smaller than the reported diameter of the coaxial BIS modified biopsy probe.<sup>[35]</sup> The smaller probe dimension allows a more effective use of the instrument and saves room for further functionalization, which is an important

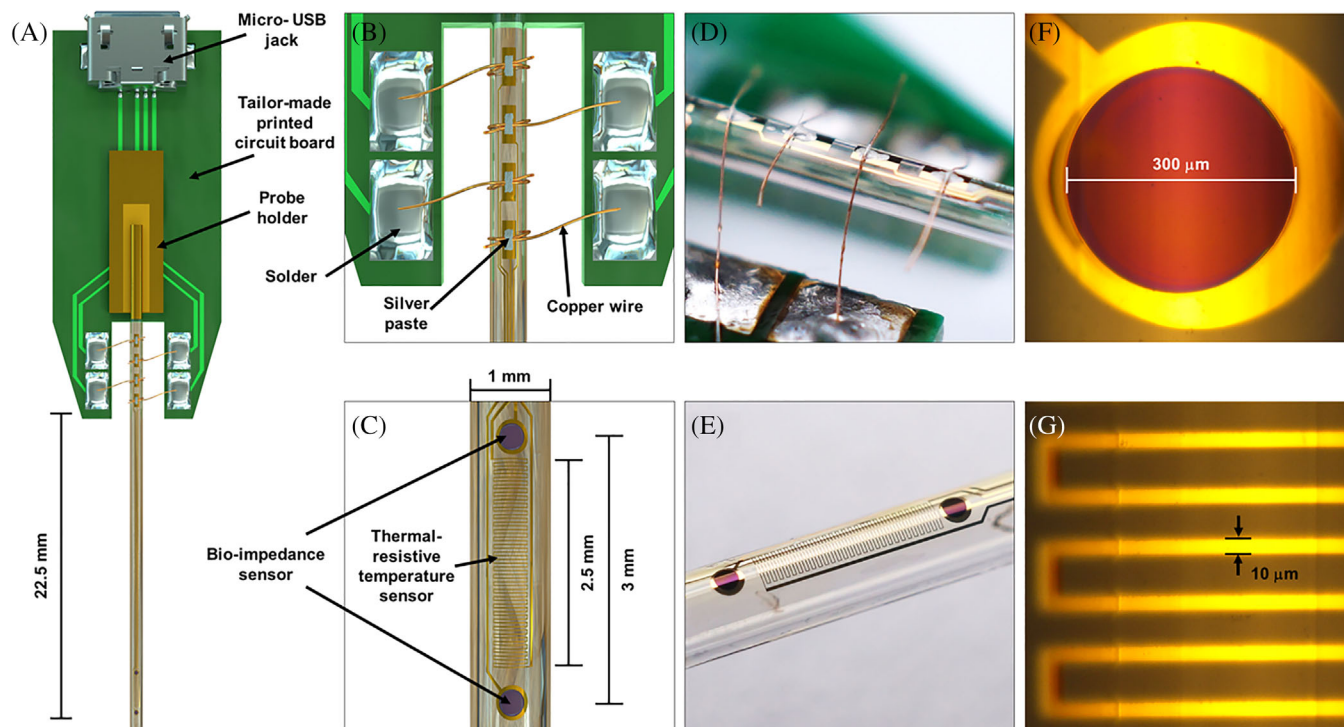


**FIGURE 1** Detailed structural schematic of the Bio-impedance and temperature sensing probe. A, Overview of the sensing probe connected with a tailor-made printed circuit board (PCB) using micro-USB jack for data collection. B, Schematic showing the connection between the sensing probe and the PCB using copper wire and silver paste. C, Schematic of the tip of the sensing probe. D, Image of the probe-PCB connection. E, Image of the tip of the sensing probe. F, Microscopic image showing the PEDOT:PSS coated micro electrode. G, Microscopic image showing the line width of the thermal-resistive temperature sensor

consideration for the clinical application. Previously, researchers have also demonstrated patterning of electrodes on the needle surface for direct impedance measurements. Jun et al. have applied interdigitated electrodes for the real-time impedance measurement of porcine muscle and fat tissues.<sup>[21,32–33]</sup> Park et al. adhered multiple metal strips on a biopsy needle surface for four electrodes measurement of the impedance of mouse liver<sup>[34]</sup> and utilized heat shrink tube for encapsulation. Although the heat shrink tube is durable and robust, it is difficult to define the electrode area precisely and leads to variations among devices in mass production. Here, we use parylene-SR as the encapsulation layer because of its excellent chemical resistance. The thin parylene-SR coating (500 nm) is highly conformal and allows measurement under different bio-medium without leakage. Figure 2 shows an exploded view of the probe. To improve the durability of the passivation layer, surface treatment with a silane primer 3-(Trimethoxysilyl)-propyl methacrylate was implemented before the parylene-SR deposition. This adhesion promotor forms covalent bonding between parylene molecules and glass; hence, the parylene coating is difficult to wear off.

As the substrate of the device is a capillary glass tube, photoresists will be difficult to be applied by spin-coating.

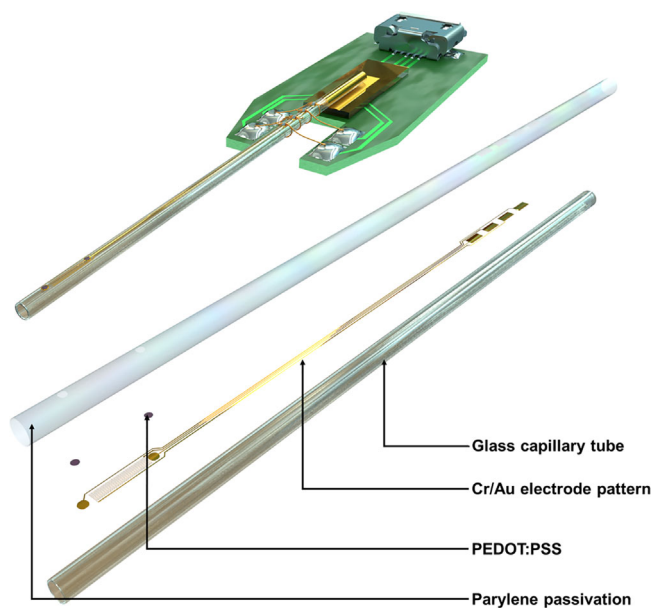


**FIGURE 2** Exploded view of the probe. The top diagram shows the completed probe illustration. The lower diagram shows the exploded view which reveal the composition of the probe: glass capillary tube, Cr/Au electrode pattern, PEDOT:PSS and parylene passivation layer

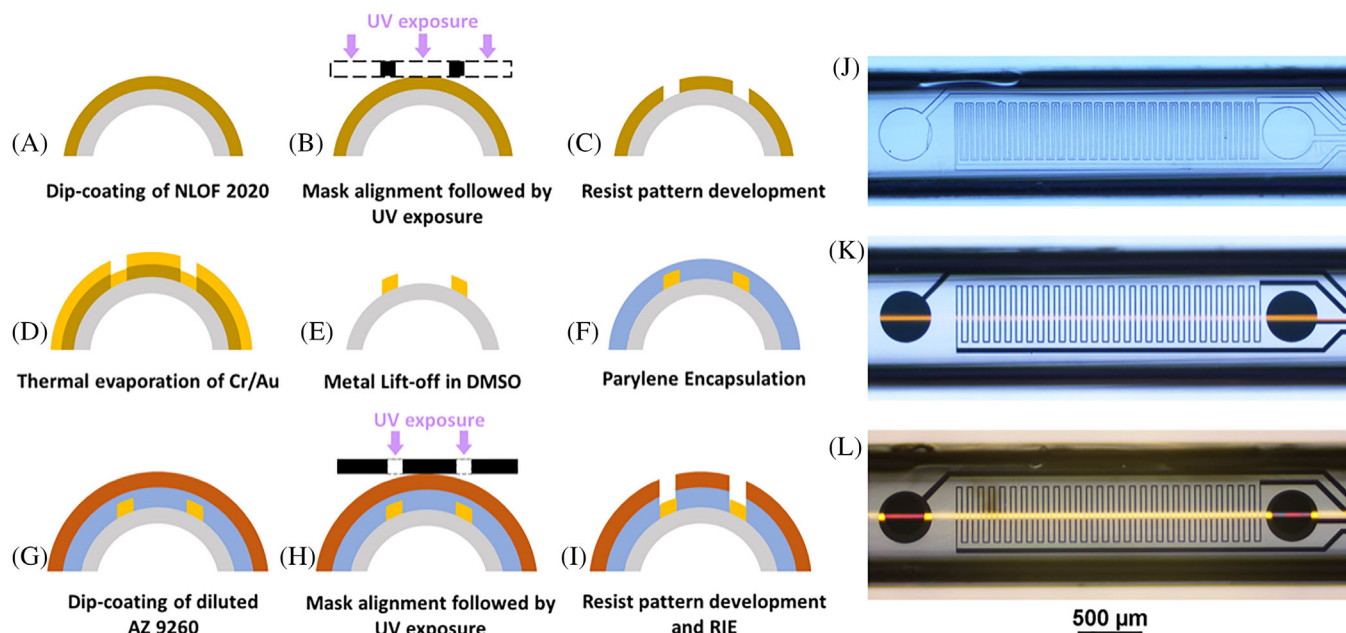


**FIGURE 3** Overall fabrication process of the probe. A, Photoresist application on the glass capillary tube by dip-coating. B, Alignment of the photomask with the tube for UV exposure. C, Development of the photoresist pattern. D, Deposition of Cr/Au by thermal evaporation. E, Lift-off process to remove non-patterned metal. F, Vapor deposition of parylene for encapsulation. G, Photoresist application by dip-coating for patterning the area to expose the working electrodes. H, Mask alignment and UV exposure process. I, After resist development, the sample underwent reactive ion etching to expose the working areas. J, Microscopic image of the capillary device after step c. K, Microscopic image of the device after step e. L, Microscopic image of the device after electropolymerization of PEDOT:PSS

Here dip-coating is employed to provide a uniform film. Details of the dip-coating setup are illustrated in Figure S1. It was modified from a syringe pump. A 3d printed holder was attached to the moving plate to hold the sample for dipping. It can achieve a constant pulling and insertion speed of around  $800 \mu\text{ms}^{-1}$ . The thickness of the coated resist film after developing was observed to be 2.1 to  $2.6 \mu\text{m}$  thick under the scanning electron microscope, as shown in Figure S2. As a flat photomask was used on cylindrical substrates, features further away from the long axis will be difficult to pattern. It is because light diffraction will happen on areas that are further away from the photomask. The electrode patterns were designed to have a total width of  $640 \mu\text{m}$  around the long axis, which the light diffraction is still tolerable for the patterning of small features down to  $10 \mu\text{m}$ . The complete fabrication process of the device is shown in Figure 3A to I. NLOF 2020 negative photoresist was used in the lithography process for patterning the electrodes. After the deposition of 50/5 nm Au/Cr metal, non-patterned metal was lift-off by dimethyl sulfoxide (DMSO). After the parylene encapsulation, a positive photoresist was used as a sacrificial layer for reactive ion etching (RIE) to expose the working electrode.

The dimensions of the impedance measurement electrodes are designed after considering the effective field coverage volume simulated by the finite element analysis

(COMSOL Multiphysics v.5.3). The significant volume was estimated using the current density magnitude  $J$  ( $\text{Am}^{-2}$ ) with a cutoff value of  $0.1 \text{ Am}^{-2}$ . Any current density lower than that was considered to have no contribution to the measurement of the total impedance. Figure S3 shows the side view and the front view of the current density distribution. The approximated significant volume is about  $0.0363 \text{ cm}^3$ , while the tumor sizes are often measured in centimeters scale.<sup>[38]</sup> For a 1 cm diameter spherical tumor, the volume is  $0.52 \text{ cm}^3$ , and the effective measurement volume of our impedance sensor is only 7% of the total volume. It confirms the impedance information measured by our probe is highly localized. It is important to mention that thermal ablation usually requires ablating an additional 5-10 mm thick margin of normal tissue surrounding the tumor to ensure there are no tumor cells left. The  $300 \mu\text{m}$  diameter electrodes adapted here can ensure the impedance measurement is localized and for precise control of the ablation process.

When the polarizable electrodes like Au are immersed into the electrolyte, an electrical double layer will form at the electrode-electrolyte interface. This layer will insert a capacitive component to the impedance system, which can be described by Gouy-Chapman-Stern (GCS) model.<sup>[39]</sup>

$$\frac{1}{C_d} = \frac{1}{C_H} + \frac{1}{C_D} \quad (1)$$

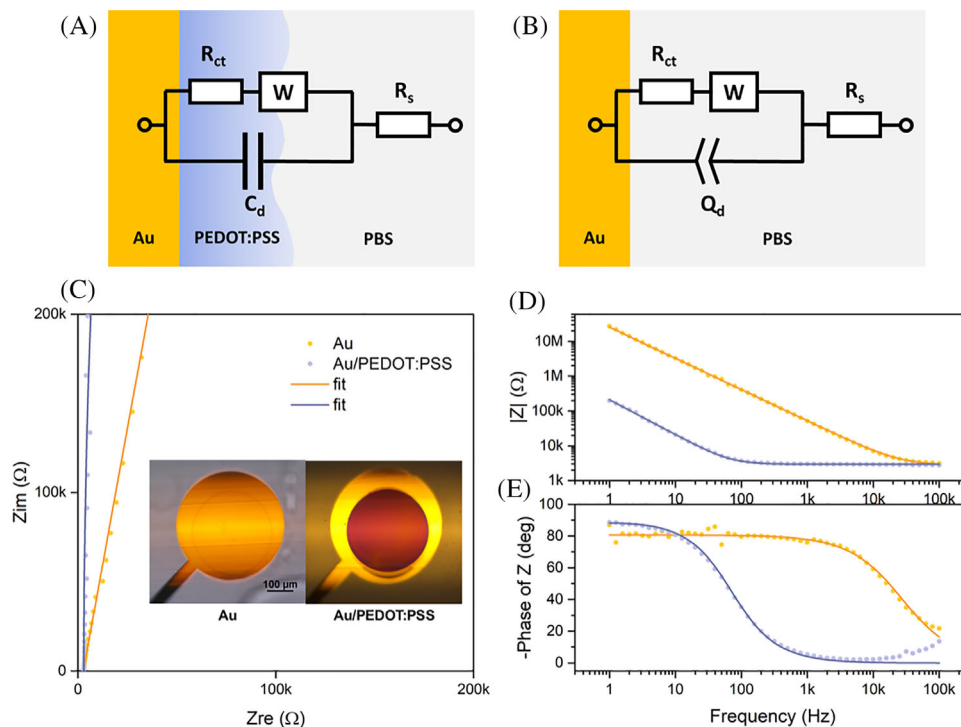


**FIGURE 4** Impedance characterization of microelectrodes. A, Randles equivalent circuit using ideal capacitor component for PEDOT:PSS coated gold electrode. B, Randles equivalent circuit using constant phase element for bare gold electrode. C, Nyquist plot of measured and fitted impedance data. Inset pictures show the microscopic image before and after the electro polymerization of PEDOT:PSS. D, Bode impedance magnitude plot. E, Bode impedance phase difference plot

where  $C_d$  is the resultant double layer capacitance,  $C_H$  is the capacitance of the charge accumulated at the outer Helmholtz plane,  $C_D$  is the capacitance of the diffusing charge. The total current passing through the working interface is the sum of both non-faradaic and faradaic double layer charging current. The non-faradaic current describes current passage by charge displacement, which can be represented by a capacitor. In comparison, faradaic current describes the passage of charges from the electrode surface to the bulk solution, which is usually modeled with a Warburg resistance in series with a charge transfer resistance. The Warburg resistance is a nonideal circuit element which can be used to describe the resistance of mass transfer, and it will change with frequency. Figure 4A and B are Randles equivalent circuit to simulate the electrical response of the double layer interface. When electrode size is small, the charge storage capacity on the electrode surface is reduced; hence, the double layer capacitance becomes small and reduces both non-faraday and faraday current passage. The small electrodes would lead to high impedance, especially at the low frequency range, which would significantly deteriorate the information at low frequency.

In order to reduce electrode impedance without enlarging actual electrode size, here, we use electropolymerization to deposit conductive polymer PEDOT:PSS onto the

exposed working electrodes and the PEDOT:PSS can create a rough surface, which increases the effective area of the working electrodes. The use of PEDOT:PSS to lower electrode impedance has been used in other fields such as neural signal measurement<sup>[40–43]</sup> for improving signal to noise ratio. In the electropolymerizing process, a galvanostatic current supply with current density  $5 \mu\text{Amm}^{-2}$  was supplied to the working electrode against a platinum counter electrode for 150 seconds. The optical image and impedance measurement of the bare gold and after the PEDOT:PSS deposition (Au/PEDOT:PSS) are shown in Figure 4C–E. For the case of Au/PEDOT:PSS, a Randles equivalent circuit in Figure 4A was used to fit the data, while for the case of the bare gold electrode (Au), the equivalent circuit in Figure 4B was used instead, where  $R_s$  is the solution resistance,  $R_{ct}$  is the charge transfer resistance,  $W$  is the Warburg resistance, and  $C_d$  is the double layer capacitance.<sup>[44–46]</sup> The only difference between the two circuits is replacement of the capacitor  $C_d$  with a constant phase element (CPE),  $Q_d$ . CPE is a component usually used to model the behavior of an imperfect capacitor, which happens in systems like rough electrode surfaces,<sup>[47]</sup> inhomogeneous reaction rates on a surface<sup>[48]</sup>, or nonuniform current distribution.<sup>[49]</sup> In the case of bare gold microelectrode on a curved surface, the current distribution is nonuniform, and the measured data is difficult to fit with

TABLE 1 Equivalent circuit model fitting parameters

	$R_s$ ( $\Omega$ )	$C_d$ (nF)	$Q^o$ (nSs <sup>n</sup> )	$n$	$W$ (Ss <sup>1/2</sup> )	$R_{ct}$ (M $\Omega$ )
Au	2792	-	7.29	0.90	2.17e-15	24.82
Au/PEDOT:PSS	2949	753.80	-	-	4.25e-8	3.46

a normal capacitor component but can fit well with CPE. The CPE component is defined by:

$$\frac{1}{Z} = Q_d(j\omega)^n \quad (2)$$

where  $Q_d$  has the numerical value of the admittance ( $1/|Z|$ ) at  $\omega = 1$  rad s<sup>-1</sup> and  $0 < n < 1$ . When  $n$  is close to 1, it resembles a capacitor. As  $Q_d$  does not have the same unit as a capacitor, they cannot be directly compared unless the value of  $n$  is large enough ( $n > 0.8$ ). The bode plots show the magnitude and phase difference of the measured impedance, while the Nyquist plot shows the real and imaginary part of the impedance. The measured range of frequency was from 1 to 100 kHz. Figure 4D shows that the overall impedance decreased after the deposition of PEDOT:PSS. At 100 Hz, the impedance decreased by 99% from 408 k $\Omega$  to 3.7 k $\Omega$ . From the phase difference plot, the system is mostly capacitive from 1 to 10 kHz for bare gold electrode. After PEDOT:PSS deposition, the system became less capacitive. The phase difference remained under 20° when the frequency was lower than 100 Hz. Note that at 1 Hz, the phase difference of the bare gold electrode cannot reach the same value as Au/PEDOT:PSS (88°) but saturated at the value of 80°. This implies that the Au/PEDOT:PSS electrode is closer to an ideal capacitor than a bare gold electrode. This lowered phase shift characteristic was described with the CPE component. The closer to ideal capacitor properties of the Au/PEDOT:PSS electrode can be further confirmed from the Nyquist plot in Figure 4C. The Au/PEDOT:PSS formed a linear curve that was more perpendicular to the x-axis, which suggested the Au/PEDOT:PSS electrode behaves closer to an ideal capacitor than the bare gold electrode. Table 1 shows the physical parameters resolved from the equivalent circuit model fitting. The double layer capacitance increased about 100 times from 7.29 to 753 nF. The polymerization charge employed in this work is 75 mCcm<sup>-2</sup>, and it is similar to the value reported before.<sup>[50]</sup> The reduction of charge transfer resistance (from 24.82 to 3.46 M $\Omega$ ) and the increase in the Warburg coefficient ( $2.17 \times 10^{-15}$  Ss<sup>1/2</sup> to  $4.25 \times 10^{-8}$  Ss<sup>1/2</sup>) are results of facilitated charge transfer and mass transfer reaction.<sup>[43,51]</sup> The PEDOT:PSS deposition time will affect the thickness of the PEDOT:PSS formation and further reduce the interface impedance. A comparison of different deposition time with electrode impedance was shown in Figure S4. A longer polymerization time reduces

the electrode impedance at the low-frequency region, and the electrode became less capacitive.

Calibration is needed for the evaluation of the temperature coefficient of resistance of the Au thin film coil temperature sensor. The relationship between the change of resistance and change of temperature is linear over a wide range of temperature and is described by the temperature coefficient of resistance (TCR),  $\alpha$ <sup>[37]</sup>

$$\alpha = \frac{\Delta R/R_0}{\Delta T} \quad (3)$$

where  $R_0$  is the initial resistance at room temperature,  $\Delta R$  is the change of coil resistance, and  $\Delta T$  is the temperature change measured from thermocouple. The TCR is calibrated experimentally by measuring the change of resistance of the thermal sensor against a commercial thermocouple.  $\Delta R/R_0$  is plotted against temperature to show the correlation. During the temperature sensor calibration, the probe was immersed into a beaker of deionized water together with a thermocouple. A hotplate was used to heat up the water from room temperature to about 65°C. When the thermocouple reading reaches 65°C, the hotplate was switched off and the beaker of water was cooled down at room temperature. A d.c. 0.5 V is supplied to the temperature sensing module, and the resistance change of the coil pattern was continuously measured at a sampling rate of 2 Hz. The whole process lasted for 1 hour, and the resistance change follows the change of temperature, as shown in Figure 5A. The value of  $\alpha$  is given by the slope of Figure 5B. The data can be fitted with a linear equation with a Pearson's R value of 0.99965 and the TCR value is  $0.00161 \pm 5.9\%$  °C<sup>-1</sup>. The error came from device-to-device variation ( $n = 5$ ). The standard deviation of the temperature measurement is about  $\pm 0.7$  °C ( $n = 120$ ).

As the impedance measurement electrodes and the temperature sensor are integrated onto the probe together, it is important to avoid crosstalk between them. Herein, a 40-channel solid-state multiplexer was used to control and turn on the electrodes used for impedance sensing or temperature sensing, while the others are kept as an open circuit. For the temperature sensing channel, a potential-static 0.5 V d.c. bias is applied, while for the impedance measuring channel, a potential-static 10 mV rms a.c. bias at 1000 Hz was used. Figure 5C shows the resistance change of the temperature sensor with a color legend mapping the corresponding converted temperature using the TCR value

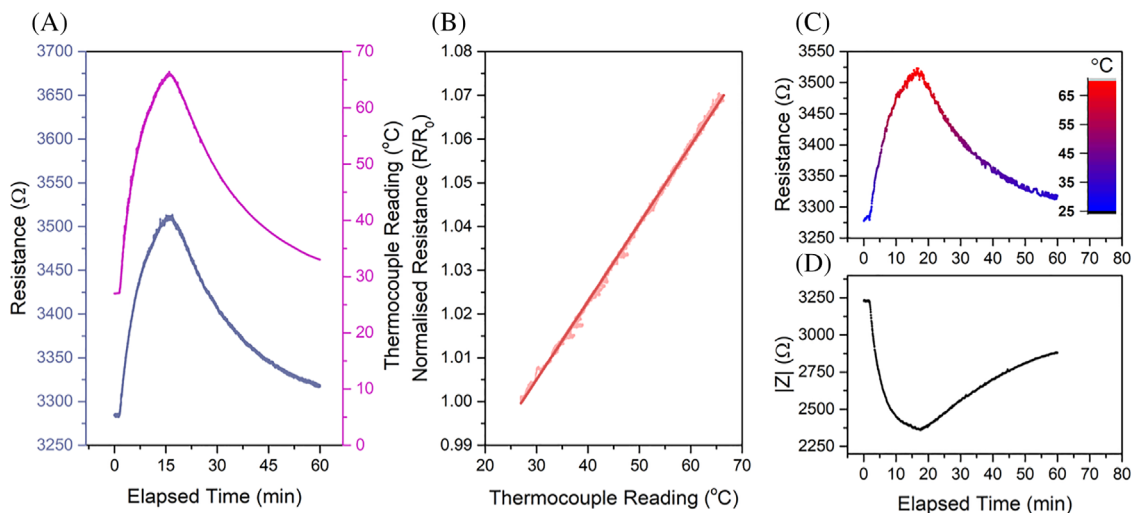


**FIGURE 5** Calibration of the bio-impedance and temperature sensing probe. A, A comparison between the change of normalized coil resistance and the change of thermocouple reading. B, Plot of  $\Delta R/R_0$  against temperature measured from thermocouple. The slope is 0.00178 which represents the temperature coefficient of resistance  $\alpha$ . Pearson's  $R = 0.99965$ . The linear equation is given as  $y = 0.00178x + 0.9515$ . C, Resistance change of the temperature sensing coil in PBS. The corresponding temperature is shown with a color mapping using the calibrated curve in b. D, Change of solution impedance as PBS solution was heated and cooled measured at 1000 Hz

obtained from Figure 5B. Simultaneously, the impedance change of the PBS solution at 1 kHz was recorded in Figure 5D. The conductivity of the PBS solution increased when the solution temperature increased, which is due to the increase of the ion mobility in the PBS solution. When the temperature returns gradually to room temperature, the conductivity of the PBS solution decreases. The change of conductivity of electrolyte with temperature can be described by the temperature coefficient of variation  $\theta$ :

$$\theta = \frac{(\kappa_{T_2} - \kappa_{T_1}) \cdot 100}{(T_2 - T_1) \cdot \kappa_{T_1}} \quad (4)$$

where  $\kappa_{T_2}$  is the conductivity at temperature  $T_2$  while  $\kappa_{T_1}$  is the conductivity at temperature  $T_1$ . The experimentally measured  $\theta$  value from 27°C to 37°C is 1.4% °C<sup>-1</sup>. The common temperature coefficient of variation of electrolyte is ranged from 1% to 3% °C<sup>-1</sup>.<sup>[52]</sup> The impedance of the PBS solution did not return to its initial value because of the evaporation of water during the heating process, and the concentration of the solution was higher than its initial state. The demonstration of the real-time impedance and temperature measurements suggests the probe is ready for the ex vivo thermal ablation testing.

The laser ablation utilized high energy, coherent and monochromatic infrared laser light source to induce localized heating on the tissues. As the light can transmit over a long distance in glass fiber with little energy loss, it can be integrated with the endoscope for minimally invasive surgery applications. When laser light is pointed to the bio-

logical tissue, scattering and absorption will occur,<sup>[53]</sup> and the laser-induced thermal therapy (LITT) actually involves the study of radiative transport considering the absorption and scattering coefficient of tissues.<sup>[54]</sup> Usually, the biological tissues are considered as turbid media, and the effective transport scattering coefficient is much larger than the absorption coefficient. As a result, the light can penetrate tissue at a certain depth. For the near-infrared radiation utilized here, the penetration depth can reach around 10 mm.<sup>[55]</sup> Studies had also shown that a higher temperature would facilitate light attenuation and local heat generation.<sup>[56–57]</sup>

The light source used is neodymium-doped yttrium aluminum garnet (Nd:YAG) emits at a wavelength of 1064 nm. Figure 6A shows a 200  $\mu$ m diameter glass fiber inserted through our impedance and temperature sensors developed capillary tube. The integrated probe was inserted into porcine liver samples cut with an average volume of 4 cm<sup>3</sup>. Figure 6B shows the insertion setup and the fixation of the laser fiber with a removable adhesive. The output power of the laser was adjusted to 2 W, the ablation period is 3 minutes. The laser-ablated porcine liver and the cross-sectional images are shown in Figure 7A. One can notice that the laser ablated area was circular in shape with 1cm diameter. The tissue color has changed to pale pink. The temperature change of the tissue sample was reflected by the resistance change of the device, which was measured and shown in Figure 7B. The real-time impedance response of the porcine liver was in Figure 7C. It can be noticed that once the ablation was started, the sample temperature increased rapidly from 27°C to about

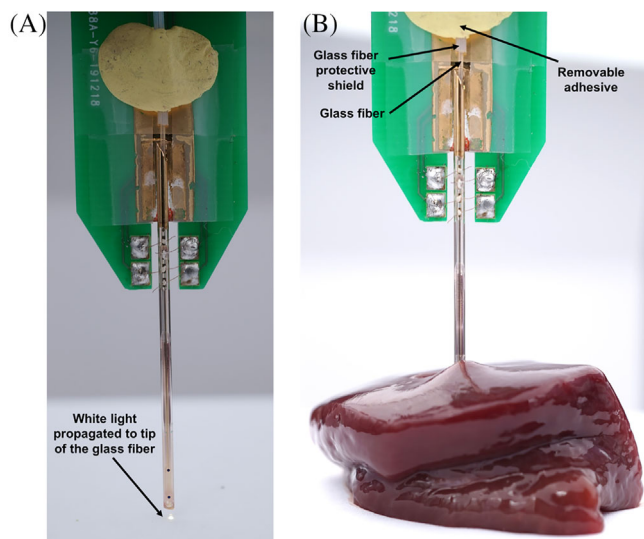


**FIGURE 6** Ex vivo porcine liver sample testing setup. A, Overall view showing insertion of glass fiber into the capillary tube and a white light propagated to the glass fiber tip for illustration. B, Insertion of the capillary probe into a piece of porcine liver tissue

75°C in less than 5 minutes. At the same time, the tissue impedance drops over 50% due to elevated ion mobility and saturates before the temperature reaches the highest point. When the temperature reaches the highest value, a sudden increase in impedance was recorded, which is three to five times higher than the original impedance. This is due to the fact that tissue dehydration and vaporization followed by carbonization and charring. This rapid dehydration would lead to a significant drop in conductance, which has been reported as “popping” in radiofrequency ablation of liver tissues.<sup>[58–60]</sup> A popping sound can be heard due to explosive tissue abruption when fluids vaporize inside the tissue and build up an intra-tissue pressure. After the laser power was switched off, the intracellular fluid surrounding the ablation site will diffuse back to the measurement area, and thus the conductance increased again. It is also noteworthy to point out that since no cooling system nor blood circulation is present in our ex vivo test, the heating on the applicator tip cannot be well dispersed and thus causes overshooting of the temperature. When the samples returned to room temperature, the final impedance reading is slightly higher than the initial value before the ablation, and it is also due to the loss of tissue fluids by vaporization of water during laser ablation. Dehydrated tissue has a lower conductivity than pristine tissue.

### 3 | CONCLUSION

In this study, we have successfully fabricated a temperature sensor and impedance sensor on a capillary tube as

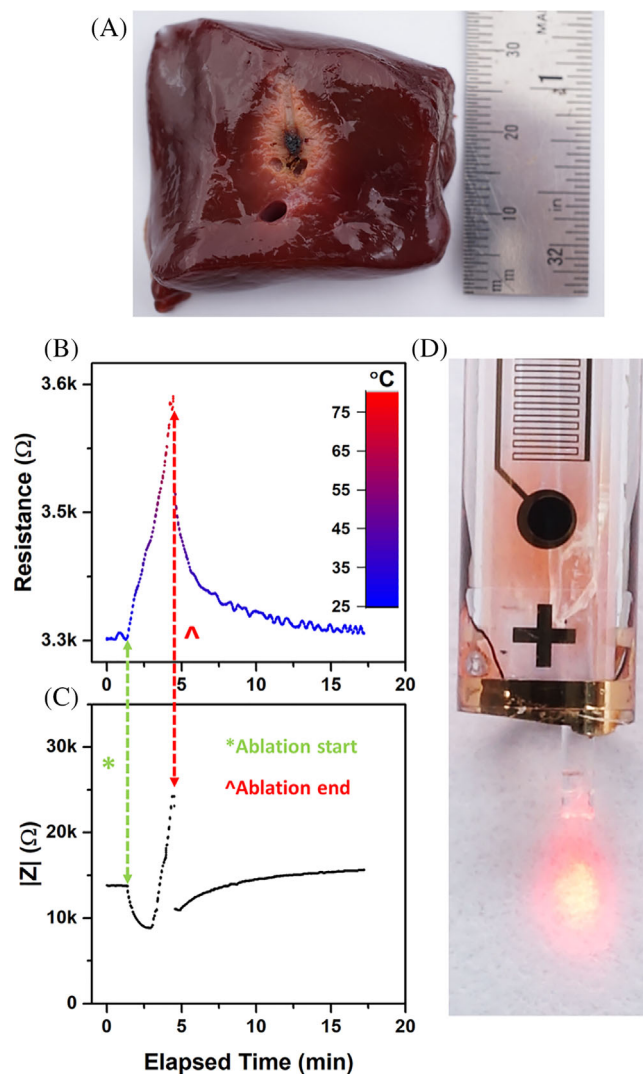


**FIGURE 7** In situ measurement of temperature and impedance of porcine liver tissue during laser ablation. A, Cross-sectional image of the ablation zone of the porcine liver sample after the laser ablation. B, Resistance measurement of the temperature sensing module with temperature color mapping. C, Impedance measurement of porcine liver tissue during the laser ablation. D, Image showing the glass fiber insertion through the capillary tube and transmitting a visible laser light

a real time monitoring tool for the thermal ablation. The electrodes impedance was lowered by a layer of electropolymerization of PEDOT:PSS. Using a multiplexer switching mechanism, real-time in situ measurement of temperature and impedance measurement is feasible. This probe is further integrated with a thermal ablation fiber to perform in situ temperature and tissue impedance monitoring during laser-induced thermal treatment on porcine liver. The probe can provide highly localized electrical and thermal information on the biological tissues or organs, which cannot easily be achieved by the conventional characterization tools. The low cost of



fabrication and user-friendly design offers great potential in clinical testing and mass production.

## 4 | EXPERIMENTAL SECTION

### 4.1 | Materials

The designed printed circuit boards were ordered from JiaLiChuang (HongKong) Co., Limited (JLPCB). All the chemicals were purchased from Sigma-Aldrich and used as received.

### 4.2 | Fabrication of temperature and impedance sensors on capillary tube surface

Lithography procedures and treatment are adopted and modified from X. D. Ji et al.<sup>[61]</sup> and A. H. Y. Lau et al.<sup>[37]</sup> 40 mm segment of glass capillary tube were trimmed and attached on a 7 mm × 13 mm glass slide using double-sided tape after cleaning procedures. The capillary tubes underwent UV Ozone treatment for 5 minutes to increase the surface energy. At 120 °C, a hexamethyldisilazane (HMDS) self-assembled monolayer (SAM) was deposited in vapor phase for promoting photoresist adhesion on the capillary tube surface. The capillary tubes were slowly dipped into and withdrawn from NLOF 2020 negative photoresist at about 800  $\mu\text{ms}^{-1}$ . Due to capillary effect, photoresist will be drawn into the capillary tube. Kim wipes were used to slowly absorb out the photoresist from the tube. After prebaking at 110 °C for 1 minute, the samples were aligned and exposed under 365 nm UV light for a dosage of 66  $\text{mJcm}^{-2}$  followed by post exposure baking at 110 °C for 1 minute. Resist pattern was developed in 2.38 wt% TMAH for 30 -40 seconds. 50 nm of gold (Au) was deposited by thermal evaporation using 5 nm chromium (Cr) as an adhesion layer. The photoresist sacrificial layer together with the metals on top were lift-off by 80 °C DMSO. The samples were then immersed into an adhesion promoter (0.5% volume ratio 3-(Trimethoxysilyl)-propyl methacrylate ( $\text{C}_{10}\text{H}_{20}\text{O}_5\text{Si}$ ) in 1:1 mixture of DI water and IPA) for 20 minutes. After drying in ambient air for 20 minutes, the samples were rinsed with IPA to remove excessive molecules. The samples then underwent a physical vapor deposition of Parylene-SR. Similar photolithograph techniques followed to pattern the passivation layer except the resist was replaced with diluted AZ9260 positive resist (10 g AZ9260 + 5.5 g PGMEA), the pre-baking time was set as 1.5 minute and the UV exposure dosage was 450  $\text{mJcm}^{-2}$ . The exposed parylene-SR was etched away by RIE using  $\text{O}_2$  gas. The fabrication steps were summarized in Figure 3.

The finished devices were connected to the PCB board using a 50- $\mu\text{m}$ -diameter copper wire. At the device end, the copper wire was connected by conductive silver paste and dried for 1 hour. At the PCB board end, the copper wire was soldered.

### 4.3 | Electro-polymerization of PEDOT:PSS

The procedure and solution recipe was adopted from Ricardo Starbird and Wolfgang Bauhofer.<sup>[62]</sup> 10 mmol  $\text{L}^{-1}$  3,4-ethylenedioxythiophene (EDOT) in 2 wt% poly(sodium-p-styrenesulfonate) (PSS) aqueous solution was used for electro-polymerization. During the deposition process, a constant current density of 5  $\mu\text{Amm}^{-2}$  was supplied to the microelectrodes using a platinum wire as the counter electrode. The deposition time was 150 seconds. A magnetic stirrer was used at around 400 rpm during the deposition process.

### 4.4 | Finite element analysis with COMSOL

All boundaries of the simulation system were insulated except the working electrodes. One electrode was given a 5 mV electrical potential while the other electrode was set as a ground potential. Domain material properties was set as isotropic with conductivity  $\sigma = 1 \text{ Sm}^{-1}$  and relative permittivity as  $\epsilon = 49.5$ .

### 4.5 | Impedance characterization and circuit fitting

For impedance spectroscopy, measurement frequency was ranged from 1 to 100 kHz with 10 mV rms potential static measurement in 0.1 M PBS solution. For single frequency real time impedance monitoring, the frequency was set at 1000 Hz. The data measurement was done with PARSTAT 3000A-DX from Princeton Applied Research. All equivalent circuit analysis was done with ZSimpWin software.

### 4.6 | Multiplexer switching

The switching mechanism was achieved by Keithley 7001 Switch System using a 20-channel 7013C multiplexer card. Only two of the 20 channels were used in this work. The switching was controlled by LabView program using a KUSB-488B GPIB cable. The system switch between the temperature sensor and impedance sensor every 2 seconds.

#### 4.7 | Temperature coefficient of resistance determination

The resistance change of the device in changing DI water temperature was compared with the measurement from a T-type thermocouple using TC-2000 thermocouple meter. The thermocouple reading was collected as analog voltage change in the range of 0-5 V. Conversion from analog voltage to temperature is given by  $v*16$  where  $v$  is the analog voltage output of the TC-2000 thermocouple meter.

#### 4.8 | Temperature coefficient of variation of PBS solution

The change of conductivity of 0.1 M PBS during temperature change was measured with the probe integrated with the multiplexer. A 0.5 V d.c. voltage was supplied to the temperature sensor and the resistance were measured at a sampling rate of 5 Hz. For the impedance sensor, 10 mV rms ac bias was supplied to the impedance sensor at 1000 Hz. The impedance response was sampled at 4 Hz.

#### 4.9 | In situ monitoring of porcine liver laser ablation

Pristine porcine liver was freshly bought and tested immediately. The liver samples were cut with a dimension of about 4 cm<sup>3</sup>. A small incision was made for better insertion of the probe into the porcine liver tissue. The laser ablation catheter was inserted through the capillary tube. The tip of the 200  $\mu$ m diameter glass fiber was about 0.5 mm exceeding the tip of the capillary tube. The laser wavelength is near infrared at 1064 nm. The power supply was set at 2 W.

#### CONFLICT OF INTEREST

The authors declare no conflict of interest.

#### DATA AVAILABILITY STATEMENT

Research data are not shared.

#### ORCID

Paddy Kwok Leung Chan  <https://orcid.org/0000-0002-3166-2192>

#### REFERENCES

1. S.Nahum Goldberg, G. Scott Gazelle, L. Solbiati, W.J. Rittman, P.R. Mueller, *Acad. Radiol.* **1996**, 3, 636.
2. J.G. Nirmala, M. Lopus, *Cell Biol. Toxicol.* **2020**, 36, 145.
3. C. Brace, *IEEE Pulse* **2011**, 2, 28.
4. M. Ahmed, C.L. Brace, F.T. Lee, Jr., S.N. Goldberg, *Radiology* **2011**, 258, 351.
5. H. Zhi-yu, L. Ping, Y. Xiao-ling, C. Zhi-gang, L. Fang-yi, Y. Jie, *Sci. Rep.* **2017**, 7, 41246.
6. S.A. Sapareto, W.C. Dewey, *Int. J. Radiat. Oncol. Biol. Phys.* **1984**, 10, 787.
7. M. Nikfarjam, V. Muralidharan, C. Christophi, *J. Surg. Res.* **2005**, 127, 208.
8. D.S.K. Lu, S.S. Raman, P. Limanond, D. Aziz, J. Economou, R. Busuttill, J. Sayre, *J. Vasc. Interv. Radiol.* **2003**, 14, 1267.
9. V.I. Shah, U. Raju, D. Chitale, V. Deshpande, N. Gregory, V. Strand, *Cancer* **2003**, 97, 1824.
10. G.A. Sonn, S. Natarajan, D.J.A. Margolis, M. MacAiran, P. Lieu, J. Huang, F.J. Dorey, L.S. Marks, *J Urol* **2013**, 189, 86.
11. E.C. Hoffer, C.K. Meador, D.C. Simpson, *J. Appl. Physiol.* **1969**, 27, 531.
12. S. Gabriel, R.W. Lau, C. Gabriel, *Phys. Med. Biol.* **1996**, 41, 2251.
13. C. Gabriel, S. Gabriel, E. Corthout, *Phys. Med. Biol.* **1996**, 41, 2231.
14. Q. Guofeng, W. Wei, D. Wei, Z. Fan, A.J. Sinclair, C.R. Chatwin, *IEEE Trans. Biomed. Eng.* **2012**, 59, 2321.
15. T.K. Bera, J. Nagaraju, G. Lubineau, *J. Vis.* **2016**, 19, 691.
16. V.S. Teixeira, J.-P. Kalckhoff, W. Krautschneider, D. Schroeder, *Curr. Dir. Biomed. Eng.* **2018**, 4, 115.
17. M.W. van der Helm, O.Y.F. Henry, A. Bein, T. Hamkins-Indik, M.J. Cronce, W.D. Leineweber, M. Odijk, A.D. van der Meer, J.C. T. Eijkel, D.E. Ingber, A. van den Berg, L.I. Segerink, *Lab. Chip* **2019**, 19, 452.
18. K. Heileman, J. Daoud, M. Tabrizian, *Biosens. Bioelectr.* **2013**, 49, 348.
19. M. Hussein, F. Awwad, D. Jithin, H. El Hasasna, K. Athamneh, R. Iratni, *Sci. Rep.* **2019**, 9, 4681.
20. F. Zhang, T. Jin, Q. Hu, P. He, *J. Electroanal. Chem.* **2018**, 823, 531.
21. J. Yun, Y.-T. Hong, K.-H. Hong, J.-H. Lee, *Sens. Actuators B Chem.* **2018**, 261, 537.
22. S.M. Moqadam, P.K. Grewal, Z. Haeri, P.A. Ingledew, K. Kohli, F. Golnaraghi, *J. Electr. Bioimpedance* **2018**, 9, 17.
23. R. W. R. L. Gajasinghe, O. Tigli, M. Jones, T. Ince, presented at 2016 IEEE SENSORS, 30 Oct.-3 Nov. 2016, **2016**.
24. A. Kekonen, M. Bergelin, M. Johansson, N. Kumar Joon, J. Bobacka, J. Viik, *Sensors (Basel)* **2019**, 19, 2505.
25. E. Kozhevnikov, X. Hou, S. Qiao, Y. Zhao, C. Li, W. Tian, *J. Mater. Chem. B* **2016**, 4, 2757.
26. B. Amin, M.A. Elahi, A. Shahzad, E. Porter, B. McDermott, M. O'Halloran, *Med. Biol. Eng. Comput.* **2019**, 57, 1.
27. A.A. Al-Ali, A.S. Elwakil, B.J. Maundy, presented at 2018 IEEE 61st International Midwest Symposium on Circuits and Systems (MWSCAS), 5-8 Aug. 2018, **2018**.
28. R.H. Bayford, *Annu. Rev. Biomed. Eng.* **2006**, 8, 63.
29. I. Milsom, R. Sivertsson, B. Biber, T. Olsson, *Clin. Physiol.* **1982**, 2, 409.
30. D.P. Bernstein, H.J.M. Lemmens, *Med. Biol. Eng. Comput.* **2005**, 43, 443.
31. B. Thompson, M.H. Drazner, D.L. Dries, C.W. Yancy, *Congestive Heart Failure (Greenwich, Conn.)* **2008**, 14, 261.
32. J. Yun, G. Kang, Y. Park, H.W. Kim, J.-J. Cha, J.-H. Lee, *Sens. Actuators B Chem.* **2016**, 237, 984.
33. J. Yun, J. Kim, J.H. Lee, *J. Vis. Exp.* **2017**, 129, 56622.

34. J. Park, W.M. Choi, K. Kim, W.I. Jeong, J.B. Seo, I. Park, *Sci. Rep.* **2018**, *8*, 264.
35. S. Halonen, J. Kari, P. Ahonen, K. Kronstrom, J. Hyttinen, *Annu. Rev. Biomed. Eng.* **2019**, *47*, 836.
36. M. John, A. Post, D.A. Burkland, B. D. Greet, J. Chaisson, G.A. Heberton, M. Saeed, A. Rasekh, M. Razavi, *Pacing. Clin. Electrophysiol.* **2020**, *43*, 593.
37. A.H.Y. Lau, G.K.K. Chik, Z. Zhang, T.K.W. Leung, P.K.L. Chan, *Adv. Intell. Syst.* **2020**, *2*, 2000005.
38. PDQ Adult Treatment Editorial Board. *Ovarian Germ Cell Tumors Treatment (PDQ®): Patient Version. 2020 Oct 9. In: PDQ Cancer Information Summaries [Internet]. Bethesda (MD): National Cancer Institute (US); 2002-. [Figure, Tumor sizes are often measured; 2020*
39. A.J. Bard, L.R. Faulkner, *Electrochemical Methods: Fundamentals and Applications*, Wiley, New York **2001**.
40. A. Schander, T. Teßmann, S. Stokov, H. Stemmann, A.K. Kreiter, W. Lang, presented at 2016 38th Annual International Conference of the IEEE Engineering in Medicine and Biology Society (EMBC), 16-20 Aug. 2016, **2016**.
41. A.S. Pranti, A. Schander, A. Bödecker, W. Lang, *Proceedings* **2017**, *1*, 492.
42. S.Y. Yang, B.N. Kim, A.A. Zakhidov, P.G. Taylor, J.K. Lee, C.K. Ober, M. Lindau, G.G. Malliaras, *Adv. Mater.* **2011**, *23*, H184.
43. X. Cui, V.A. Lee, Y. Raphael, J.A. Wiler, J.F. Hetke, D.J. Anderson, D.C. Martin, *J. Biomed. Mater. Res.* **2001**, *56*, 261.
44. M. Sheliakina, A.B. Mostert, P. Meredith, *Adv. Funct. Mater.* **2018**, *28*, 1805514.
45. A.S. Karimullah, D.R.S. Cumming, M. Riehle, N. Gadegaard, *Sens. Actuators B. Chem.* **2013**, *176*, 667.
46. D.D. Macdonald, *Electrochim. Acta* **2006**, *51*, 1376.
47. W.H. Mulder, J.H. Sluyters, T. Pajkossy, L. Nyikos, *J. Electroanal. Chem. Interf. Electrochem.* **1990**, *285*, 103.
48. C.-H. Kim, S.-I. Pyun, J.-H. Kim, *Electrochim. Acta* **2003**, *48*, 3455.
49. J.-B. Jorcin, M.E. Orazem, N. Pébère, B. Tribollet, *Electrochim. Acta* **2006**, *51*, 1473.
50. J. Bobacka, A. Lewenstam, A. Ivaska, *J. Electroanal. Chem.* **2000**, *489*, 17.
51. T. Chung, J.Q. Wang, J. Wang, B. Cao, Y. Li, S.W. Pang, *J. Neural Eng.* **2015**, *12*, 056018.
52. R.B. Campbell, C.A. Bower, L.A. Richards. *Soil Science Society of America Journal*, **1949**, *13*, 66.
53. W.F. Cheong, S.A. Prael, A.J. Welch, *IEEE J. Quantum Electron.* **1990**, *26*, 2166.
54. M. J. C. v. G. A. J. Welch, *Optical-Thermal Response of Laser-Irradiated Tissue*, Springer, Dordrecht, **1995**.
55. T.J. Farrell, M.S. Patterson, B. Wilson, *Med. Phys.* **1992**, *19*, 879.
56. M.G. Skinner, S. Everts, A.D. Reid, I.A. Vitkin, L. Lilge, M.D. Sherar, *Phys. Med. Biol.* **2000**, *45*, 1375.
57. J.P. Ritz, A. Roggan, C.T. Germer, C. Isbert, G. Müller, H.J. Buhr, *Laser. Surg. Med.* **2001**, *28*, 307.
58. M.L. Fernandes, C.-C. Lin, C.-J. Lin, W.-T. Chen, S.-M. Lin, *J. Vasc. Interv. Radiol.* **2010**, *21*, 237.
59. H. Iida, T. Aihara, S. Ikuta, N. Yamanaka, *World J. Gastroenterol.* **2012**, *18*, 5870.
60. T.J. Vogl, M.G. Mack, A. Roggan, R. Straub, K.C. Eichler, P.K. Müller, V. Knappe, R. Felix, *Radiology* **1998**, *209*, 381.
61. X. Ji, P. Zhou, L. Zhong, A. Xu, A.C.O. Tsang, P.K.L. Chan, *Adv. Sci.* **2018**, *5*, 1701053.
62. R. Starbird, W. Bauhofer, M. Meza-Cuevas, W.H. Krautschneider, Effect of experimental factors on the properties of PEDOT-NaPSS galvanostatically deposited from an aqueous micellar media for invasive electrodes, The 5th 2012 Biomedical Engineering International Conference, Muang, Thailand, **2012**, pp. 1-5, <https://doi.org/10.1109/BMEiCon.2012.6465500>

## SUPPORTING INFORMATION

Additional supporting information may be found online in the Supporting Information section at the end of the article.

**How to cite this article:** T.K.W. Leung, X. Ji, B. Peng, G.K.K. Chik, D.S.H.S. Dai, G. Fang, T. Zhang, X. Cheng, K.W. Kwok, A.C.O. Tsang, G.K.K. Leung, P.K.L. Chan. *Nano Select* **2021**, *1*.  
<https://doi.org/10.1002/nano.202100041>